NANO LETTERS

Letter

Cite This: Nano Lett. 2018, 18, 520−527

pubs.acs.org/NanoLett

Chiral Metamaterials of Plasmonic Slanted Nanoapertures with Symmetry Breaking

Yang Chen, Jie Gao,* and Xiaodong Yang*

Department of Mechanical and Aerospace Engineering, Missouri University of Science and Technology, Rolla, Missouri 65409, United States

Supporting Information

ABSTRACT: We propose a universal design scheme for a new type of chiral metamaterials based on plasmonic slanted nanoapertures simply milled in a single metal layer. Strong optical chirality is introduced by tilting nanoapertures with almost arbitrary shape along a certain direction to break all the mirror symmetries. As a typical example, chiral metamaterial based on slanted split-ring apertures is demonstrated with giant circular dichroism in transmission (CDT) over 78% at 760 nm. We reveal that the high CDT originates from the circularly dichroic mode coupling process in the slanted nanoapertures induced by spin-dependent field overlap conditions. Furthermore, tunable CDT is presented through the in-plane rotation of nanoapertures to form chiral images with controllable image contrast. Besides, chiral metamaterials with slanted nanoapertures of two other shapes including L-shaped aperture and rectangular aperture are also presented with large circular dichroism. We envision that our demonstrated chiral metamaterials enable promising platforms for a variety of applications in nonlinear optics, chiral imaging and sensing, spectroscopy, and polarization manipulation.

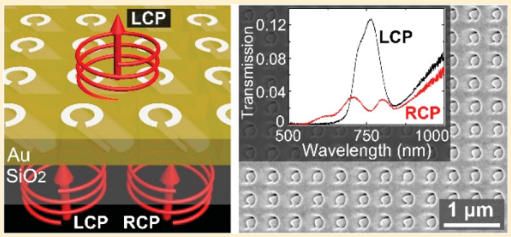

KEYWORDS: *Chiral metamaterial, circular dichroism, 3D fabrication, mode coupling, plasmonics*

Chirality is a ubiquitous phenomenon in nature, ranging from amino acids, to our hands, and even to galaxies in the universe, which refers to the geometric property of an object lacking any mirror plane or inversion symmetry. Chiral materials usually appear in two enantiomeric forms, which are mirror symmetric and cannot coincide with each other by simple rotation or translation. The structural chirality results in optical chirality with differential optical response to left-handed and right-handed circularly polarized (LCP and RCP) light. Despite its great significance in chemical and biological research,[1,2] optical chirality is, however, extremely weak for natural materials. As a solution, chiral metamaterials developed in recent years are able to enhance the chiroptical effects by several orders of magnitude,[3−7] promising potential applications in ultrasensitive biosensing,[8,9] miniature circular polarizer,[10,11] negative refractive index materials,[12,13] and nonlinear optics.[14,15]

Although three-dimensional (3D) chiral metamaterials usually exhibit strong optical chirality, their fabrication is inherently incompatible with two-dimensional (2D) patterning techniques. In order to solve this challenging issue, several top-down fabrication methods have been developed, but each method still suffers from certain limitations. For the femtosecond direct laser writing method,[3,16,17] the fabricated structures usually possess the micrometer-scale spatial resolution due to the diffraction limit, so that this method cannot be applied to make nanoscale structures operating in the visible or near-infrared spectrum. For the focused ion or electron beam induced deposition method,[18,19] the low material deposition rates in general limit the structure fabrication throughput and large-scale production. In the glancing-angle deposition technique,[20,21] although the parallel deposition process is fast, the achievable structure morphologies are limited as column-based posts, chevrons and spirals. For both the on-edge lithography[22] and stacking lithography,[23,24] the lithography facilities with high-resolution alignment are required and the fabrication process is usually complex. Meanwhile, bottom-up fabrication techniques using DNA, cysteine, and peptide as self-assembly templates have also been utilized[25−27] but their flexibility and reproducibility is seriously restricted. To overcome the fabrication difficulties of 3D chiral metamaterials, chiral metasurfaces, as the 2D version of chiral metamaterials, have been extensively proposed to break the in-plane mirror symmetry by using planar structures such as gammadions,[28] split-rings[29,30] and G-shaped structures.[31] However, these planar structures are not truly chiral and they suffer from weak chiroptical responses in the linear regime, although their nonlinear chirality can be much stronger.[32,33]

In this work, we report a new type of chiral metamaterials based on plasmonic slanted nanoapertures milled in a single thick metal layer. The fundamental design principle is to break all the mirror symmetries of the nanoaperture by tilting it along a certain direction. This type of chiral metamaterials can be easily fabricated using one-step tilted-angle focused ion beam

Received: October 23, 2017
Revised: November 21, 2017
Published: December 5, 2017

ACS Publications © 2017 American Chemical Society

DOI: 10.1021/acs.nanolett.7b04515
Nano Lett. 2018, 18, 520−527

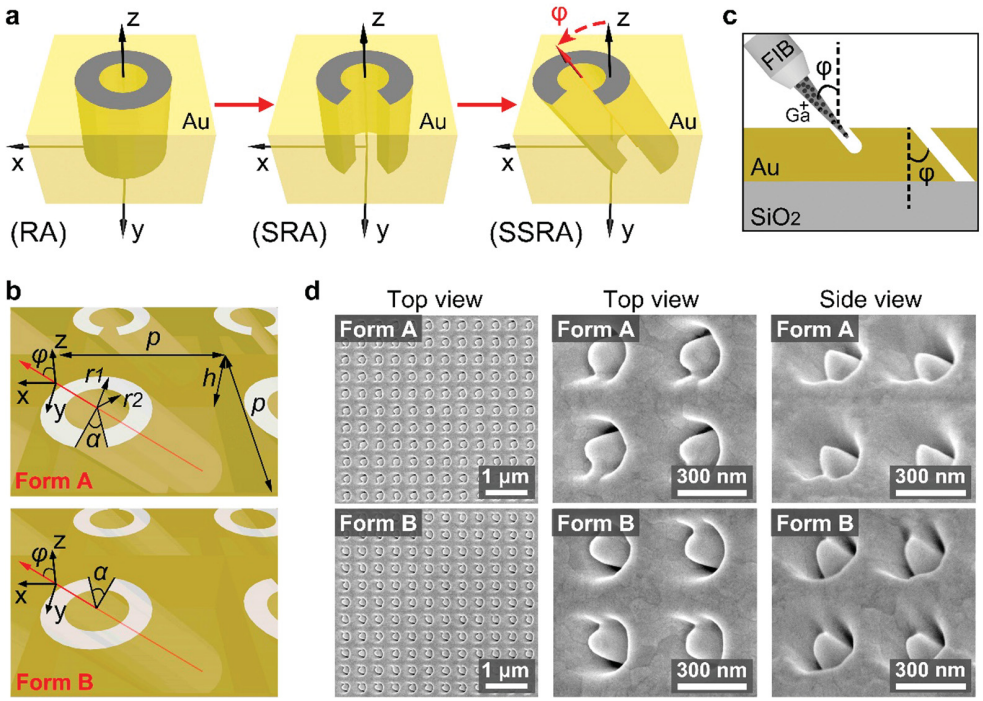

Figure 1. (a) Schematics of the transformation process from a ring aperture (RA) to a split-ring aperture (SRA) and then to a slanted split-ring aperture (SSRA). (b) Sketches of the two forms of SSRA chiral metamaterial with geometrical parameters labeled. (c) Illustration of the fabrication process with tilted-angle FIB. (d) SEM images of the fabricated SSRA chiral metamaterials in Form A and Form B with a slant angle of 40° (side view images are captured with a visual angle of 52° to the surface normal).

(FIB) milling process. Without loss of generality, chiral metamaterial with slanted split-ring aperture (SSRA) array is proposed and discussed as one example. Giant circular dichroism in transmission (CDT) over 78% is experimentally demonstrated in the near-infrared wavelength range. Distinguished from other types of chiral metamaterials and metasurfaces, the high CDT of SSRA chiral metamaterial results from the spin-dependent mode coupling process inside nanoapertures induced by circularly dichroic field overlap conditions. To further elucidate the mechanism of optical chirality, optical power flow and electric near-field distributions are mapped and compared under different circular polarization incidence. After that, the CDT of SSRA chiral metamaterial is presented to be adjustable over a wide range through the in-plane rotation of nanoapertures, leading to chiral images with controllable image contrast. Apart from the SSRA nanostructure, slanted L-shaped aperture and slanted rectangular aperture are also considered as two other typical examples to construct chiral metamaterials with large circular dichroism. Our demonstrated chiral metamaterials composed of plasmonic slanted nanoaperture array promise a powerful platform for many exciting applications in nonlinear optics, chiral imaging and sensing, chiral spectroscopy, and polarization manipulation.

As shown in Figure 1a, the SSRA structure in a single thick metal layer is evolved from an ordinary ring aperture (RA) that possessing mirror symmetry in all the three orthogonal planes (i.e., $x-y$, $x-z$, and $y-z$ plane) without optical chirality. By converting the ring aperture into an achiral split-ring aperture (SRA), the mirror symmetry of $x-z$ plane is broken and the mirror symmetry of the other two planes is preserved. Further tilting in $x-z$ plane transforms the split-ring aperture into a slanted split-ring aperture (SSRA) lacking any mirror symmetry. By arranging the SSRA structures in a 2D periodic array, 3D chiral metamaterial is constructed as depicted in Figure 1b. It exists in two enantiomer forms (Form A and Form B) that are mirror symmetric with each other relative to $x-z$ plane. Note that we will primarily discuss Form A below. Different from other types of chiral metamaterials that require complicated fabrication procedures, the SSRA chiral metamaterial can be easily fabricated using one-step tilted-angle focused ion beam milling.[34,35] By simply tilting the sample substrate relative to the ion beam, slanted nanoapertures with arbitrary shapes are milled obliquely into the gold film with high uniformity (see Methods). The slant angle φ of apertures is determined by the angle between the sample surface normal and the incident direction of ion beam as illustrated in Figure 1c. SEM images of the fabricated SSRA chiral metamaterials in Form A and Form B are depicted in Figure 1d (more details in Supporting Information S1).

In order to examine the chiroptical properties of the SSRA metamaterial, full-wave electromagnetic simulations are performed. The outer and inner radius of the ring $r1$ and $r2$ are fixed as 120 and 70 nm. The split angle α, slant angle φ, gold film thickness h, and period p are optimized as 40°, 30°, 180, and 400 nm, respectively (see Supporting Information S2). Circularly polarized light is illuminated vertically on the substrate. As shown in Figure 2a, a broad transmission resonance at 1030 nm is observed for both LCP and RCP incidence in Form A. Such a resonance also appears in the SRA structure without slant angle and it is attributed to the excitation of the fundamental mode in aperture.[36] Because of the geometrical chirality of the SSRA structure, the fundamental mode of the LCP case is moderately stronger than that of the RCP case. Consequently, circular dichroism in transmission CDT = $(T_{LCP} - T_{RCP})/(T_{LCP} + T_{RCP})$ is calculated to be nearly constant around 0.2 over a broad

DOI: 10.1021/acs.nanolett.7b04515
Nano Lett. 2018, 18, 520−527

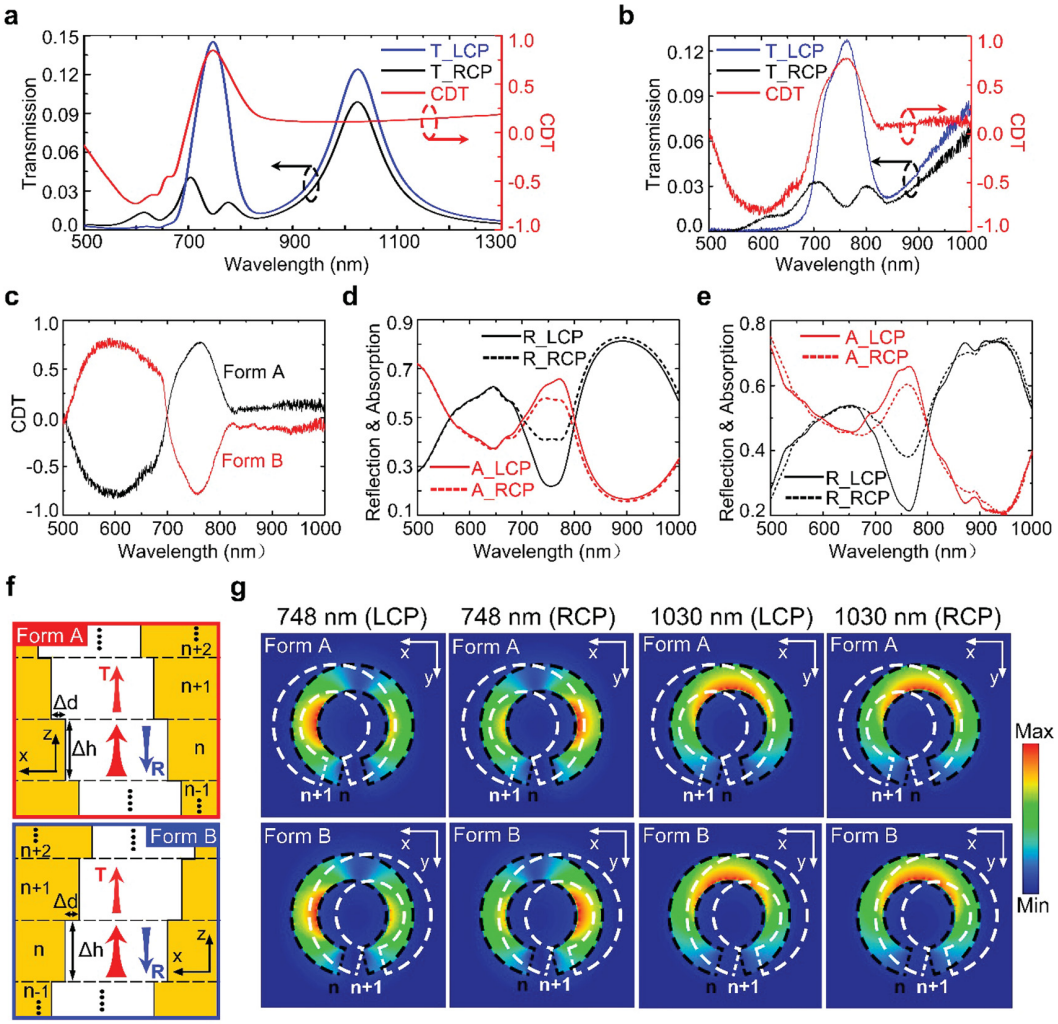

Figure 2. (a) Simulated and (b) measured transmission spectra of the SSRA chiral metamaterial in Form A under LCP (T_LCP) and RCP (T_RCP) incidence and the corresponding CDT spectra. (c) Measured CDT spectra of the two forms of SSRA metamaterials. (d) Simulated and (e) measured reflection spectra (R_LCP and R_RCP) and absorption spectra (A_LCP and A_RCP) for Form A under LCP and RCP illumination. (f) Illustration of the analysis model considering the slanted aperture as a series of cascaded waveguide segments. (g) Electric field amplitude $|E|$ distributions of the propagation mode in the waveguide segment n of split-ring aperture under LCP and RCP incidence at 748 and 1030 nm, with displacement of the segment $n + 1$ outlined.

spectrum from 860 to 1500 nm. Meanwhile, another pronounced plasmonic resonance is also presented at 748 nm under LCP incidence, whereas the transmission under RCP incidence is strongly suppressed there to form a sharp CDT resonance as large as 0.85, accompanied by a high Q-factor of 9.7. We are primarily interested in such a strong CDT resonance in the following contents. Although the CDT around 600 nm is large as well, the transmission is very low.

The experimental results match well with the simulations as shown in Figure 2b, where the remaining deviations mainly arise from fabrication tolerances and undesired light scattering of surface defects. Nevertheless, a maximum CDT of 0.78 is still realized at 760 nm in experiment, which is much larger than most of the existing chiral metamaterials and metasurfaces with CDT around 0.4 or even lower.[5,19,24,28,37,38] Aperture-type metamaterials have an apparent advantage over particle-type ones in that they can efficiently suppress the background illumination to achieve a high signal-to-noise ratio. To further inspect the chirality of SSRA metamaterial, the CDT spectra of its two enantiomers are measured and compared in Figure 2c showing opposite CD response as expected. The polarization state of the transmitted wave is analyzed in Supporting Information S3.

Generally, circular dichroism originates from the distinct responses of absorption and scattering to circularly polarized light with the opposite handedness. For most of the plasmonic chiral metamaterials and metasurfaces, circular dichroism in absorption is the dominant factor, benefiting from photon-spin sensitive near-field distributions and the corresponding ohmic loss in metal.[38−40] To reveal the underlying mechanism of high CDT in the SSRA metamaterial, reflection and absorption spectra are simulated and measured in Figure 2d,e. It is shown that the spin-dependent difference in reflection and absorption contributes to the CDT resonance. Compared to the RCP case, more incoming LCP wave is coupled into the metamaterial in Form A indicated by the weaker reflection and more dissipation is then produced during the LCP mode propagation through the slanted apertures with the stronger absorption. Because the difference in reflection is much larger than that in absorption, higher transmission is still achieved under LCP illumination.

DOI: 10.1021/acs.nanolett.7b04515
Nano Lett. 2018, 18, 520−527

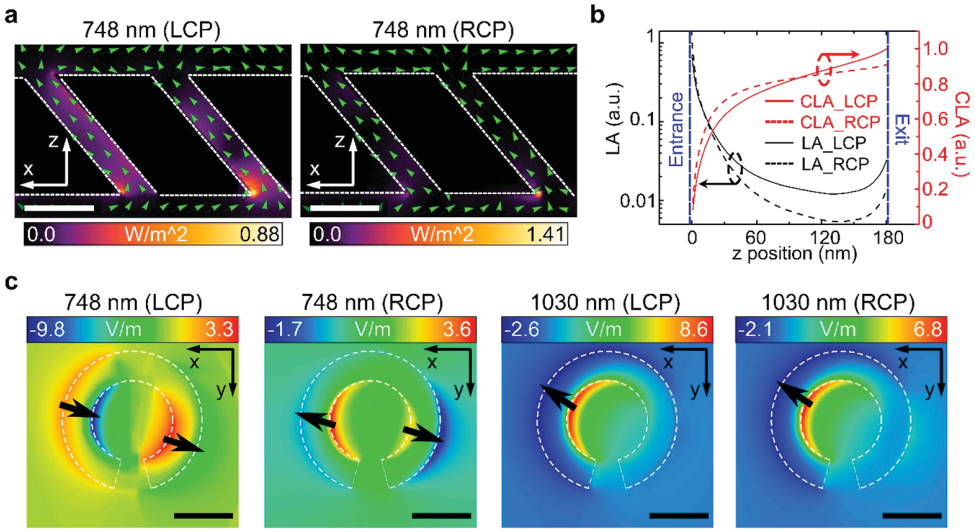

Figure 3. (a) Optical power flow distributions at 748 nm for Form A under LCP and RCP illumination (the background colors and field arrows indicate the magnitude and direction of the Poynting vector respectively, scale bar: 100 nm). (b) Layer absorption (LA) and cumulative layer absorption (CLA) distributed along the vertical z-direction (the y-coordinate of LA is in logarithmic scale). (c) Longitudinal electric field component E_z distributions plotted 4 nm above the exit plane at 748 and 1030 nm with its sign indicating the direction (scale bar: 100 nm). The black arrows show the local dipoles.

Meanwhile, most of the incident RCP wave is either reflected or dissipated, leaving the transmission channel strongly inhibited, which is another important reason for the large CDT.

Next, we are to go a step further and elucidate the origin of the difference in reflection and transmission. Distinguished from chiral metasurfaces, the SSRA metamaterial has no sense of optical twist of the incident wave at its entrance plane. Thus, the intensities of the reflected wave right from the entrance plane for LCP and RCP illumination are identical, as well as the intensities of the wave coupled into the metamaterial. However, the subsequent propagation of the coupled wave along slanted apertures is circularly dichroic. As illustrated in Figure 2f, a slanted aperture can be modeled as a series of cascaded waveguide segments with a constant displacement Δd in positive (or negative) x direction for Form A (or B).[41] The displacement Δd is determined by the slant angle φ and the length of a single segment Δh, which is far smaller than the aperture thickness h. At the interface of two connected segments, the propagation wave is reflected or transmitted depending on the mode coupling process there. Simulation results in Figure 2g illustrate that the mode distribution of split-ring waveguide at 748 nm is mainly localized at its left (right) part for the LCP (RCP) case. Therefore, compared to the RCP mode, the LCP mode in the waveguide segment n possesses a better optical field overlap with the segment $n + 1$ that is positively displaced in Form A. Consequently, more incoming LCP wave is transmitted at the segment interface and the reflection is suppressed.[42,43] Such a coupling difference induced by field overlap is further validated by the simulations described in Supporting Information S4. As the coupled mode travels from the entrance plane of the metamaterial to the exit plane, the mode coupling difference for LCP and RCP cases is continually accumulated in transmission and reflection. As a result, the remarkable CDT resonance is generated at 748 nm. On the other hand, the reflected waves from all the segment interfaces are more intensive for the RCP mode, which propagate back and emerge out of the entrance plane of nanoapertures. Because the direct reflection from the entrance plane is spin-independent, the overall reflection of the metamaterial in Form A is higher under RCP incidence than LCP incidence. For the sake of comparison, we also plot the mode distributions at 1030 nm, where the electric field is confined at the middle part of the split-ring aperture and only shows a tiny shift to the left (right) for the LCP (RCP) case. Hence the CDT induced by different mode coupling process is low at 1030 nm. As for the enantiomer Form B, the CD properties are reversed owing to the negative displacement Δd between the waveguide segments.

We proceed to clarify the influence of the excitation handedness on the optical power flow distributions at the CDT resonance. As shown in Figure 3a, the simulation results clearly display that the incoming LCP light is focused into and transmitted efficiently through the slanted aperture, resulting in the enhanced transmission. In contrast, the incident RCP light coupled into the SSRA experiences strong reflection due to the mismatch between the displacement Δd and the mode distribution of waveguide segments, as discussed before. As a result, the coupled mode is attenuated rapidly and the optical energy is confined near the entrance plane. By integrating volume absorption over x−y layers at different z-positions, the layer absorption (LA, with 100% as the maximum) of RCP is calculated to be larger at the entrance and then decays faster than that of LCP (Figure 3b), which is in agreement with the power flow distributions. The cumulative layer absorption (CLA) calculated by $\mathrm{CLA}(z) = \int_0^z \mathrm{LA}(z_0)\mathrm{d}z_0$ shows that over 37% and 64% of the total absorption takes place at the initial 5 and 20 nm for RCP incidence, while the corresponding percentage is 27% and 54% for LCP incidence. Accordingly, although the overall absorption under LCP and RCP incidence has a relatively small difference, its longitudinal distributions are highly polarization-dependent. Stemming from the different transmission process, electric field distributions at the exit plane are circularly dichroic as shown in Figure 3c. Two local dipoles in phase are observed for the LCP case at 748 nm, leading to the constructive interference in far field, while two dipoles out of phase with weaker amplitudes are suggested for the RCP

DOI: 10.1021/acs.nanolett.7b04515
Nano Lett. 2018, 18, 520−527

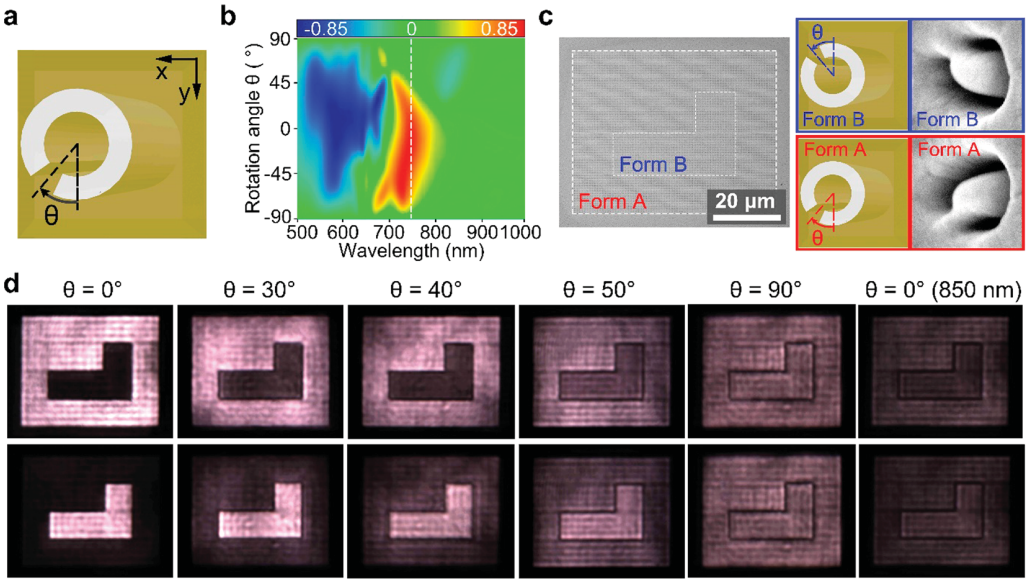

Figure 4. (a) Schematic of the SSRA structure in Form A with in-plane rotation. (b) Simulated CDT spectra of the SSRA metamaterial with varying rotation angle θ. (c) SEM image of the "L" pattern with its boundary outlined. The outer and inner areas consist of SSRA elements with the same rotation angle θ in Form A and Form B, respectively. Magnified SEM images of the two enantiomers are also presented. (d) Transmission images of multiple "L" patterns consisting of SSRA elements with different rotation angles under LCP (Row 1) and RCP (Row 2) illumination. The first five pairs are taken at 760 nm and the last pair are taken at 850 nm.

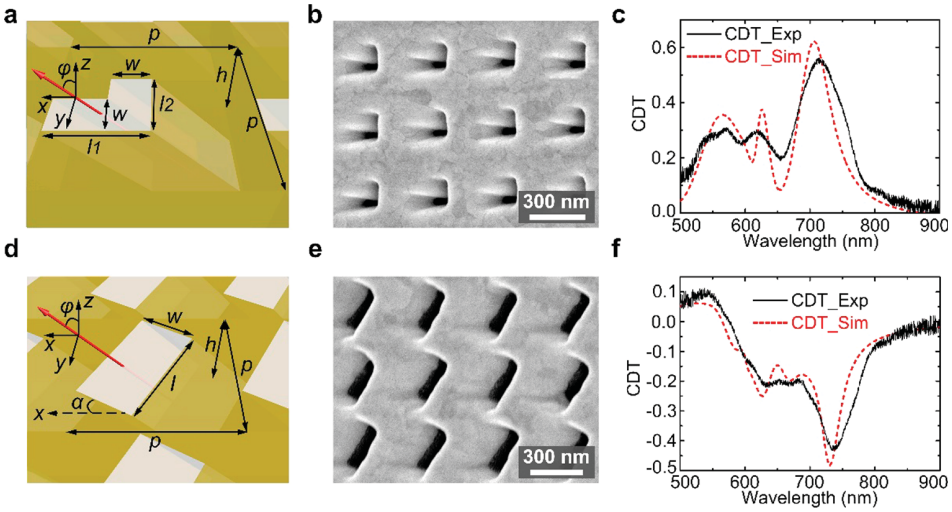

Figure 5. (a) Schematic, (b) SEM image, and (c) simulated and experimental CDT spectra of the slanted L-shaped nanoaperture array with optimized structural parameters (w = 80 nm, $l1$ = 180 nm, $l2$ = 140 nm, φ = 45°, p = 370 nm, h = 180 nm). (d) Schematic, (e) SEM image, and (f) simulated and experimental CDT spectra of the slanted rectangular nanoaperture array with optimized design (w = 160 nm, l = 320 nm, φ = 45°, α = 30°, p = 410 nm, h = 180 nm).

case, resulting in the destructive interference. Therefore, strong CDT is obtained at 748 nm for the SSRA metamaterial. By contrast, the near-field patterns at the exit plane are almost identical for LCP and RCP excitations at 1030 nm with one single local dipole, except that the magnitude of the single dipole for LCP illumination is slightly larger to generate a limited CDT.

In many applications such as chiral imaging and optical beam manipulation, chiral metamaterials with arbitrarily controllable circular dichroism is highly desired. The variation of circular dichroism usually requires delicate adjustment of multiple structural parameters of metamaterials. However, our metamaterial design provides a convenient and effective way to tune the circular dichroism through the in-plane rotation of SSRA structures with an angle θ while keeping the slant angle and direction fixed, as illustrated in Figure 4a. For θ = 0°, the existence of the metal split with its orientation normal to the tilted plane breaks the mirror symmetry of x−z plane, giving the strongest CDT. When the metal split rotates away from this position, the CDT is gradually weakened and finally disappears at θ = 90° once the metal split is parallel to the x−z plane. Simulation results in Figure 4b confirm that the CDT at 748 nm can be modulated continuously from −0.85 to 0.85 by changing the rotation angle θ. Then we demonstrate experimentally the excellent performance of SSRA metamaterial in chiral imaging to realize tunable image contrast in a wide

DOI: 10.1021/acs.nanolett.7b04515
Nano Lett. 2018, 18, 520−527

range. As shown in Figure 4c, the letter "L" is patterned using both enantiomeric forms A and B in the outer and inner regions, respectively. Image contrast is defined as $C_{AB} = (I_A - I_B)/(I_A + I_B)$, where I_A (I_B) represents the brightness of the area of Form A (Form B). Taken in transmission mode at 760 nm, C_{AB} of LCP illumination is reduced from 0.76, 0.57, 0.46, 0.24 all the way to 0 with the increasing rotation angle θ from 0° to 90°, as depicted in Figure 4d. The chiral images are inverted when illuminated by RCP light. We also capture images at 850 nm with rotation angle 0°, which exhibit image contrast of 0.15 in agreement with the CDT spectrum. Accordingly, the variation of wavelength provides an alternative way to adjust the image contrast.

To further testify the effectiveness of this new design scheme for chiral metamaterials, we give two other typical examples in Figure 5: L-shaped nanoapertures with no mirror symmetry and rectangular nanoapertures with two symmetric planes. For L-shaped nanoapertures, tilting in any direction is able to obtain chirality. A maximum CDT of 0.56 is achieved experimentally at 715 nm with tailored structural parameters. As to rectangular nanoapertures, the slant direction α is set to 30° relative to its short edge, resulting in a maximum CDT of 0.43 at 738 nm (more details in Supporting Information S7). By analogy, nanoapertures with more symmetric planes can also be transformed to chiral metamaterials using the current design method. There are no restrictions on the shape of nanoapertures, except that it cannot be circularly symmetric. The critical guideline is that the slant direction should be staggered away from all the mirror symmetric planes of the nanoaperture.

Plasmonic nanoapertures with specific shapes have unique characteristics, such as enhanced near field,[44] strong second harmonic generation,[45] wavelength-selective response[46] and high sensitivity to refractive index change.[47] The universal adaptability of the proposed design scheme of plasmonic slanted apertures makes it possible to combine these unique optical properties with chirality for realizing many promising applications. For instance, the plasmonic slanted apertures formed by tilting the achiral vertical apertures such as split ring slits[14] or rectangular holes[45] along certain directions will also acquire strong chiral-dependent optical nonlinearity under vertical illumination, which can serve as not only spin-selective nonlinear frequency converters but also ultrasensitive platforms for structural symmetry probing. Furthermore, active media such as polymer with high optical nonlinearity[48] can be infiltrated into the plasmonic slanted apertures for enhanced chiral nonlinear harmonic generations. The plasmonic slanted apertures also have the advantage of strong coupling with biomolecules within the aperture volume for sensing different types of chiral molecular structures.[49] Another example is to use multiple-sized plasmonic slanted apertures such as bowties[46] to sort incident photons into different channels at nanoscale depending on the wavelength and spin of photons, which can be applied for on-chip multiplexed chiral photodetection. Moreover, spin-switchable photonic devices with the controlled amplitude and/or phase profiles can be realized based on the plasmonic slanted apertures, such as integrated structured beam converters[50] and holographic plates.[51]

In summary, a new scheme to design and fabricate chiral metamaterials has been introduced by tilting nanoapertures along a certain direction to break all the mirror symmetries. As one typical implement, chiral metamaterial based on plasmonic SSRA structures fabricated in a single thick gold layer is presented to exhibit giant circular dichroism in transmission at near-infrared spectrum. The origin of the high CDT is explained explicitly with circularly dichroic mode coupling process between waveguide segments in nanoaperture. In addition, the SSRA metamaterial displays high flexibility in tuning the CDT continuously in a broad range through the in-plane rotation of nanoapertures, providing an effective approach to form chiral images. Our design method can be generalized into other shapes of nanoapertures with two representative examples of slanted L-shaped aperture and slanted rectangular aperture, paving the way to applications in multifunctional optical devices, optical information processing, chiral imaging, and sensing.

Methods. *Simulations.* All simulations are conducted using finite element solver COMSOL Multiphysics. The permittivity of gold is taken from spectroscopic ellipsometry data fitted with a general oscillator model and the refractive index of SiO_2 is set to 1.45. The simulation unit is enclosed by periodic boundary conditions at x- and y-directions. Perfectly matched layers (PMLs) surrounded by scattering boundary are employed along the z-direction. A circularly polarized plane wave is incident vertically on the structure.

Sample Fabrication. A 180 nm-thick gold film is deposited on a SiO_2 substrate using electron-beam evaporation. Then slanted nanoapertures are milled in the gold film using focused ion beam system (FEI Helios Nanolab 600, 30 kV, 9.7 pA). To achieve the desired slant angle φ, the sample stage is tilted relative to the ion source according to the relation shown in Figure 1c. The ion beam focus and astigmatism is finely optimized. Note that the fabricated structure is laterally extended by a factor of $1/\cos(\varphi)$ along the slant direction compared to the original pattern, which should be considered in the FIB pattern design.

Optical Characterization. To measure the transmission spectra and CDT spectra, a collimated broadband tungsten-halogen source is converted to circularly polarized wave by a combination of a linear polarizer and an achromatic quarter-wave plate and then focused normally onto the sample using a 20× objective lens. The transmitted light is collected by another 20× objective lens and directed to a spectrometer (Horiba, iHR 550). A transparent glass substrate is utilized to normalize the transmission spectra. To measure the reflection spectra, the circularly polarized light is directed through a beam splitter and focused on the sample using a 20× objective lens. Then the reflected wave is collected by the same objective and deflected by the beam splitter to a spectrometer. A reflective silver mirror is used as a reference to normalize the reflection spectra. In the chiral imaging experiments, the incident beam with tunable wavelengths is generated by a femtosecond Ti:Sapphire oscillator (Spectra-Physics Tsunami). The transmission image is adjusted by a 4-f system and captured by a charge-coupled device camera. All the optical characterization setups are illustrated in Figure S8 of Supporting Information.

■ ASSOCIATED CONTENT

Supporting Information

The Supporting Information is available free of charge on the ACS Publications website at DOI: 10.1021/acs.nanolett.7b04515.

SEM images of slanted split-ring apertures, optimization of the SSRA chiral metamaterial, analysis of the polarization state of the transmitted wave, simulations of mode coupling difference, distributions of optical

DOI: 10.1021/acs.nanolett.7b04515
Nano Lett. 2018, 18, 520−527

power flow, layer absorption and cumulative layer absorption at 1030 nm, SEM images and chiroptical analysis of slanted L-shaped aperture array and slanted rectangular aperture array, illustrations of optical characterization setups (PDF)

AUTHOR INFORMATION

Corresponding Authors

*E-mail: (J.G.) gaojie@mst.edu.
*E-mail: (X.Y.) yangxia@mst.edu.

ORCID

Jie Gao: 0000-0003-0772-4530
Xiaodong Yang: 0000-0001-9031-3155

Author Contributions

The manuscript was written through contributions of all authors. All authors have given approval to the final version of the manuscript.

Notes

The authors declare no competing financial interest.

ACKNOWLEDGMENTS

The authors acknowledge support from the Office of Naval Research under Grant N00014-16-1-2408, and the National Science Foundation under Grant ECCS-1653032 and DMR-1552871. The authors thank the facility support from the Materials Research Center at Missouri S&T. The authors also thank D. Rosenmann and D. A. Czaplewski at the Argonne National Laboratory for the gold film deposition. This work was performed in part at the Center for Nanoscale Materials, a U.S. Department of Energy, Office of Science, Office of Basic Energy Sciences User Facility under Contract No. DE-AC02-06CH11357.

REFERENCES

(1) Cintas, P. *Angew. Chem., Int. Ed.* **2002**, *41*, 1139−1145.
(2) Barron, L. D. *Molecular light scattering and optical activity*; Cambridge University Press: 2004.
(3) Gansel, J. K.; Thiel, M.; Rill, M. S.; Decker, M.; Bade, K.; Saile, V.; von Freymann, G.; Linden, S.; Wegener, M. *Science* **2009**, *325*, 1513−1515.
(4) Park, H. S.; Kim, T. T.; Kim, H. D.; Kim, K.; Min, B. *Nat. Commun.* **2014**, *5*, 5435.
(5) Cui, Y.; Kang, L.; Lan, S.; Rodrigues, S.; Cai, W. *Nano Lett.* **2014**, *14*, 1021−1025.
(6) Fang, Y.; Verre, R.; Shao, L.; Nordlander, P.; Kall, M. *Nano Lett.* **2016**, *16*, 5183−5190.
(7) Wang, Z.; Jing, L.; Yao, K.; Yang, Y.; Zheng, B.; Soukoulis, C. M.; Chen, H.; Liu, Y. *Adv. Mater.* **2017**, *29*, 1700412.
(8) Lu, F.; Tian, Y.; Liu, M.; Su, D.; Zhang, H.; Govorov, A. O.; Gang, O. *Nano Lett.* **2013**, *13*, 3145−3151.
(9) Ben-Moshe, A.; Maoz, B. M.; Govorov, A. O.; Markovich, G. *Chem. Soc. Rev.* **2013**, *42*, 7028−7041.
(10) Zhao, Y.; Belkin, M. A.; Alu, A. *Nat. Commun.* **2012**, *3*, 870.
(11) Ji, R.; Wang, S. W.; Liu, X.; Chen, X.; Lu, W. *Nanoscale* **2016**, *8*, 14725−14729.
(12) Zhang, S.; Park, Y.-S.; Li, J.; Lu, X.; Zhang, W.; Zhang, X. *Phys. Rev. Lett.* **2009**, *102*, 023901.
(13) Plum, E.; Zhou, J.; Dong, J.; Fedotov, V.; Koschny, T.; Soukoulis, C.; Zheludev, N. *Phys. Rev. B: Condens. Matter Mater. Phys.* **2009**, *79*, 035407.
(14) Ren, M.; Plum, E.; Xu, J.; Zheludev, N. I. *Nat. Commun.* **2012**, *3*, 833.
(15) Rodrigues, S. P.; Lan, S.; Kang, L.; Cui, Y.; Panuski, P. W.; Wang, S.; Urbas, A. M.; Cai, W. *Nat. Commun.* **2017**, *8*, 014602.
(16) Thiel, M.; Rill, M. S.; von Freymann, G.; Wegener, M. *Adv. Mater.* **2009**, *21*, 4680−4682.
(17) Radke, A.; Gissibl, T.; Klotzbücher, T.; Braun, P. V.; Giessen, H. *Adv. Mater.* **2011**, *23*, 3018−3021.
(18) Esposito, M.; Tasco, V.; Cuscunà, M.; Todisco, F.; Benedetti, A.; Tarantini, I.; Giorgi, M. D.; Sanvitto, D.; Passaseo, A. *ACS Photonics* **2015**, *2*, 105−114.
(19) Esposito, M.; Tasco, V.; Todisco, F.; Cuscuna, M.; Benedetti, A.; Scuderi, M.; Nicotra, G.; Passaseo, A. *Nano Lett.* **2016**, *16*, 5823−5828.
(20) Yeom, B.; Zhang, H.; Zhang, H.; Park, J. I.; Kim, K.; Govorov, A. O.; Kotov, N. A. *Nano Lett.* **2013**, *13*, 5277−5283.
(21) Mark, A. G.; Gibbs, J. G.; Lee, T.-C.; Fischer, P. *Nat. Mater.* **2013**, *12*, 802.
(22) Dietrich, K.; Lehr, D.; Helgert, C.; Tünnermann, A.; Kley, E. B. *Adv. Mater.* **2012**, *24*, OP321−OP325.
(23) Liu, N.; Liu, H.; Zhu, S.; Giessen, H. *Nat. Photonics* **2009**, *3*, 157−162.
(24) Hentschel, M.; Schaferling, M.; Metzger, B.; Giessen, H. *Nano Lett.* **2013**, *13*, 600−606.
(25) Shemer, G.; Krichevski, O.; Markovich, G.; Molotsky, T.; Lubitz, I.; Kotlyar, A. B. *J. Am. Chem. Soc.* **2006**, *128*, 11006−11007.
(26) Zhu, Z.; Liu, W.; Li, Z.; Han, B.; Zhou, Y.; Gao, Y.; Tang, Z. *ACS Nano* **2012**, *6*, 2326−2332.
(27) Chen, C.-L.; Zhang, P.; Rosi, N. L. *J. Am. Chem. Soc.* **2008**, *130*, 13555−13557.
(28) Kuwata-Gonokami, M.; Saito, N.; Ino, Y.; Kauranen, M.; Jefimovs, K.; Vallius, T.; Turunen, J.; Svirko, Y. *Phys. Rev. Lett.* **2005**, *95*, 227401.
(29) Li, Z.; Zhao, R.; Koschny, T.; Kafesaki, M.; Alici, K. B.; Colak, E.; Caglayan, H.; Ozbay, E.; Soukoulis, C. M. *Appl. Phys. Lett.* **2010**, *97*, 081901.
(30) Mutlu, M.; Akosman, A. E.; Serebryannikov, A. E.; Ozbay, E. *Opt. Lett.* **2011**, *36*, 1653−1655.
(31) Valev, V.; Smisdom, N.; Silhanek, A.; De Clercq, B.; Gillijns, W.; Ameloot, M.; Moshchalkov, V.; Verbiest, T. *Nano Lett.* **2009**, *9*, 3945−3948.
(32) Valev, V.; Silhanek, A.; Verellen, N.; Gillijns, W.; Van Dorpe, P.; Aktsipetrov, O.; Vandenbosch, G.; Moshchalkov, V.; Verbiest, T. *Phys. Rev. Lett.* **2010**, *104*, 127401.
(33) Kang, L.; Rodrigues, S. P.; Taghinejad, M.; Lan, S.; Lee, K. T.; Liu, Y.; Werner, D. H.; Urbas, A.; Cai, W. *Nano Lett.* **2017**, *17*, 7102−7109.
(34) Ndao, A.; Belkhir, A.; Salut, R.; Baida, F. I. *Appl. Phys. Lett.* **2013**, *103*, 211901.
(35) Lv, J.; Khoo, E. H.; Leong, E. S. P.; Hu, L.; Jiang, X.; Li, Y.; Luo, D.; Si, G.; Liu, Y. J. *Nanotechnology* **2017**, *28*, 225302.
(36) Alaridhee, T.; Ndao, A.; Bernal, M. P.; Popov, E.; Fehrembach, A. L.; Baida, F. I. *Opt. Express* **2015**, *23*, 11687−11701.
(37) Wang, Z.; Wang, Y.; Adamo, G.; Teh, B. H.; Wu, Q. Y. S.; Teng, J.; Sun, H. *Adv. Opt. Mater.* **2016**, *4*, 883−888.
(38) Khanikaev, A. B.; Arju, N.; Fan, Z.; Purtseladze, D.; Lu, F.; Lee, J.; Sarriugarte, P.; Schnell, M.; Hillenbrand, R.; Belkin, M. A.; Shvets, G. *Nat. Commun.* **2016**, *7*, 12045.
(39) Fedotov, V.; Schwanecke, A.; Zheludev, N.; Khardikov, V.; Prosvirnin, S. *Nano Lett.* **2007**, *7*, 1996−1999.
(40) Zhao, Y.; Alù, A. *Phys. Rev. B: Condens. Matter Mater. Phys.* **2011**, *84*, 205428.
(41) Farahani, M.; Granpayeh, N.; Rezvani, M. *J. Opt. Soc. Am. B* **2012**, *29*, 1722−1730.
(42) Yariv, A.; Yeh, P. *Photonics: optical electronics in modern communications*; Oxford University Press: New York, 2007; Vol. *6*.
(43) Carretero-Palacios, S.; García-Vidal, F. J.; Martín-Moreno, L.; Rodrigo, S. G. *Phys. Rev. B: Condens. Matter Mater. Phys.* **2012**, *85*, 035417.
(44) Jin, E. X.; Xu, X. *Appl. Phys. Lett.* **2006**, *88*, 153110.
(45) van Nieuwstadt, J. A.; Sandtke, M.; Harmsen, R. H.; Segerink, F. B.; Prangsma, J. C.; Enoch, S.; Kuipers, L. *Phys. Rev. Lett.* **2006**, *97*, 146102.

DOI: 10.1021/acs.nanolett.7b04515
Nano Lett. 2018, 18, 520−527

(46) Chen, Y.; Chu, J.; Xu, X. *ACS Photonics* **2016**, *3*, 1689−1697.
(47) Yanik, A. A.; Cetin, A. E.; Min, H.; Alp, A.; S Hossein, M.; Alexander, K.; Connor, J. H.; Gennady, S.; Hatice, A. *Proc. Natl. Acad. Sci. U. S. A.* **2011**, *108*, 11784−11789.
(48) Li, G.; Chen, S.; Pholchai, N.; Reineke, B.; Wong, P. W.; Pun, E. Y.; Cheah, K. W.; Zentgraf, T.; Zhang, S. *Nat. Mater.* **2015**, *14*, 607−612.
(49) Hendry, E.; Carpy, T.; Johnston, J.; Popland, M.; Mikhaylovskiy, R.; Lapthorn, A.; Kelly, S.; Barron, L.; Gadegaard, N.; Kadodwala, M. *Nat. Nanotechnol.* **2010**, *5*, 783−787.
(50) Zeng, J.; Li, L.; Yang, X.; Gao, J. *Nano Lett.* **2016**, *16*, 3101−3108.
(51) Wan, W.; Gao, J.; Yang, X. *ACS Nano* **2016**, *10*, 10671−10680.

DOI: 10.1021/acs.nanolett.7b04515
Nano Lett. 2018, 18, 520−527